Exploring Metal Nanoclusters for Lithium−Oxygen Batteries

Meihua Lu, Jianglan Qu, Qiaofeng Yao, Chaohe Xu, Yi Zhan, Jianping Xie, and Jim Yang Lee*

Department of Chemical and Biomolecular Engineering, National University of Singapore, 10 Kent Ridge Crescent, Singapore 119260, Singapore

ⓢ Supporting Information

ABSTRACT: α-MnO_2 nanowires modified with dispersed poly(3,4-ethylenedioxythiophene)-protected Au and Ag nanoclusters (Au−MnO_2 and Ag−MnO_2) were used for the first time as hybrid oxygen electrocatalysts for nonaqueous lithium−oxygen batteries. The Au−MnO_2 and Ag−MnO_2 hybrid catalysts surpassed the performance of pristine α-MnO_2 nanowires in full-cell tests in the following order: Au−MnO_2 > Ag−MnO_2 > pristine α-MnO_2. Specifically, cells with the Au−MnO_2 catalyst could reduce the discharge/charge overpotentials at 100 mA g^{-1} to 0.23/1.02 V and deliver discharge/charge capacities of 5784/5020 mAh g^{-1}. They could also be cycled for at least 60 times at the depth of discharge of 1000 mAh g^{-1}. The good full cell performance demonstrated the effectiveness of Au/Ag nanoclusters in promoting oxygen electrocatalysis on α-MnO_2; forming discharge products with more reactive morphologies. It is therefore worthwhile to explore the use of Au and Ag nanoclusters in other catalyst systems for oxygen electrocatalysis in nonaqueous solutions.

KEYWORDS: lithium−oxygen batteries, gold nanocluster, silver nanocluster, manganese dioxide, oxygen electrocatalyst
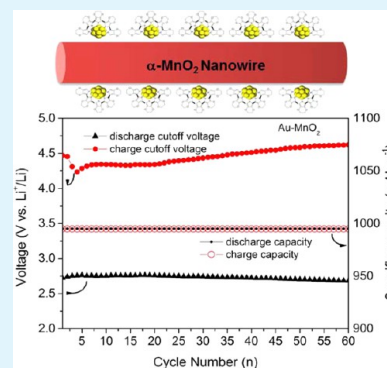
1. INTRODUCTION

Electric vehicles and grid-scale load balancing require energy storage systems much higher in specific energy than what can be provided by lithium-ion batteries, the most advanced rechargeable batteries available today.[1] Li−O_2 batteries (LOBs) are considered as a promising alternative owing to their exceedingly high theoretical specific energy. When only the weight of lithium is considered, and oxygen is supplied from the surrounding air, a nonaqueous LOB can deliver a specific energy of 11 680 Wh kg^{-1}, which is close to that of gasoline (13 000 Wh kg^{-1}).[2,3] The sluggish kinetics of the oxygen evolution reaction (OER) and the oxygen reduction reaction (ORR) in the air electrode, however, can severely undermine the practical performance resulting in low actual capacity, low round-trip energy efficiency, and poor cycle life. The limitation is in principle solvable by using an effective catalyst system. Many catalyst systems have been examined including noble metals and their derivatives,[4−10] transition metal oxides,[11−19] carbon materials,[20−26] and metal nitrides.[27,28] Among them, the noble metals have shown the best intrinsic activities for ORR and OER in aqueous and nonaqueous solutions. LOBs with PtAu nanoparticles (NPs) as the cathode catalyst could be charged at a relatively low voltage (an average of ∼3.6 V vs Li^+/Li) and achieved a round-trip energy efficiency of 73% (at a current density of 100 mA g_{carbon}^{-1}).[4] The charge voltage could be reduced even further, to as low as 3.17 V vs Li^+/Li by using Ru NPs.[8] The use of noble metals is, however, unsustainable in view of their natural scarcity, which leads to excessively high costs.

One way to increase the utilization of noble metals is to reduce them to even smaller than NPs. Nanoclusters (NCs) are ultrasmall NPs (≤2 nm) containing, typically, several to a few hundred atoms, which make them closer to molecules than NPs. NCs also tend to adopt different atomic packing than their bulk or nanoparticle counterparts. For example, Au and Au NPs normally still exhibit a face centered cubic structure, whereas a typical cluster such as $Au_{25}(SR)_{18}$ (∼1 nm in size) contains a 13-atom Au_{13} icosahedral core and a 12-atom $Au_{12}(SR)_{18}$ shell. The small size results in strong quantum confinement effects, and the energy levels in nanoclusters are even more discretized than their nanoparticle counterparts.[29] Consequently, there have been reports on NCs possessing much higher catalytic activities than bulk or NPs in oxygen and water-splitting reactions.[30−33] For example, although bulk Au and large Au NPs have not shown any OER or ORR activity, Au NCs display ORR activity in 0.1 M KOH when their size is smaller than 1.7 nm and the limiting current continues to increase with decreasing NCs size.[30,33] The catalytic activity has been attributed to the large fraction of low coordination number surface atoms, which promote facile O_2 adsorption and hence reduce the activation barrier in ORR.[30] Ag NCs with a size of 0.7 nm are also more catalytic active towards ORR than 3.3 nm Ag NPs in 0.1 M KOH.[34] While these studies have demonstrated higher activities of noble metal NCs relative to their nanoparticle counterparts for oxygen electrocatalysis in aqueous solution, there has yet to be a study to confirm the activities of NCs in nonaqueous solution where LOBs are operating. There are probably two reasons for the lack of studies on oxygen electrocatalysis by noble metal NCs in nonaqueous environment. The first reason is the degradation or
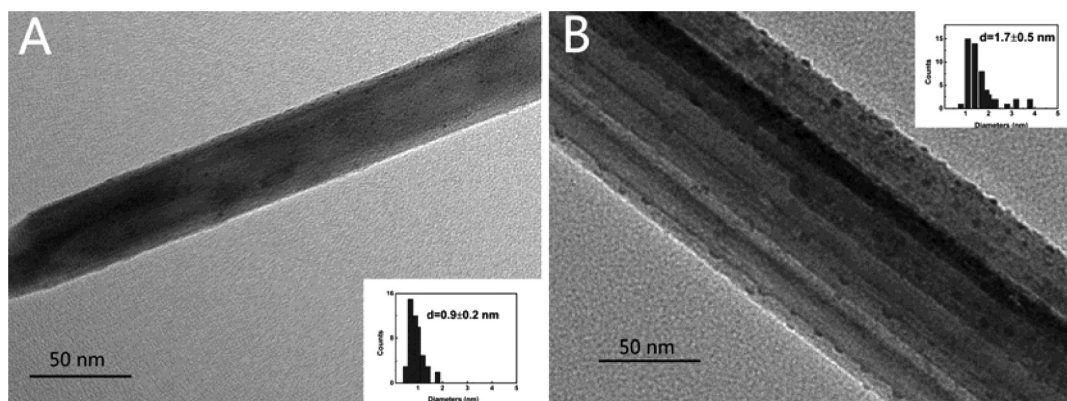
Figure 1. High resolution TEM images of (A) Au−MnO$_2$ and (B) Ag−MnO$_2$. The insets are histograms of NC size distributions.

a total loss of catalytic activity due to the propensity for NC aggregation during the electrode preparation for a nonaqueous environment. Second, most conventional NCs are prepared with thiol capping groups. The bonding of sulfur to the NC surface, which is needed for NC stabilization, is also a cause of catalyst deactivation.[33]

One possible way to address the application issues of noble metal NCs is to stabilize them on a suitable catalyst support and to select the capping agent prudently. It would even be better if the catalyst support is also catalytically active. α-MnO$_2$ nanowire (NW) could be such a support, as it has the best performance among MnO$_x$ catalysts for the LOBs. Its good performance is due to its unique 2 × 2 tunnel structure that can concurrently accommodate Li$^+$ and O$_2^{2-}$ ions.[13] In addition, there have been studies (in aqueous solution) that showed enhanced ORR and OER performance when Au NPs are combined with MnO$_x$.[35−37] The local interaction between Au NPs and MnO$_x$ was postulated to be the cause.[37] Similarly, hybrids of Ag NPs with Mn$_x$O$_y$ also demonstrated enhanced ORR and OER activities in alkaline solution.[38,39] It should be emphasized again that all of these studies were carried out in an aqueous environment. Nonaqueous LOBs have the added problem of insoluble discharge products. The cathode catalyst must also contain sufficient porosity to prevent the blockage of catalyst active sites. A catalyst support formed by NWs can provide the porous skeleton for the cathode to accommodate the solid discharge products.

This is a report of our design and preparation of NC-based catalysts for ORR and OER in nonaqueous LOBs. The hybrid catalyst was prepared by anchoring poly(3,4-ethylenedioxythiophene) (PEDOT)-capped noble metal NCs on α-MnO$_2$ NWs. Au NCs and Ag NCs were chosen in this study as the model system in view of their relatively low cost among the noble metals, and their demonstrated catalytic activities in aqueous systems. EDOT served the dual function of a reducing agent and a capping agent. EDOT is a weak reductant. It is also much bulkier in size compared with common thiol capping agents, and hence the protected NCs would have more free and accessible surface sites even after capping with PEDOT (vide infra). The Au/Ag NC-MnO$_2$ NW cathode catalysts were also tested in a full LOB cell setup. The hybrid catalysts delivered good full-cell performance, including lower charge and discharge overpotentials, higher capacity, and greater cycle stability than the pristine MnO$_2$ NWs.

2. RESULTS AND DISCUSSION

In this study, the Au and Ag clusters were synthesized under the assistance of a sulfur-containing heterocyclic compound, EDOT. EDOT served as the reducing agent for the Au and Ag precursors as well as a weak capping agent for the metal nanoclusters formed. The Au and Ag NCs were attached to the sulfur atom in the thiophene ring of the EDOT. Because the lone pair electrons of sulfur are conjugated to the thiophene ring, the coordination power of sulfur to the surface metal atoms of the NCs was significantly weakened. During the NC preparation, the reduction of the noble metal precursor also oxidatively polymerized EDOT into a conducting polymer (PEDOT). The overall electrical conductivity of the NCs was improved as a result, which should benefit the charge transfer during discharge and charge reactions. The PEDOT molecule is bulkier than most sulfur-containing capping agents (e.g., alkanethiols). The size of PEDOT, and the weaker bonding of sulfur in PEDOT to the metal surface atoms, should increase the accessibility and availability of more NC surface atoms for O$_2$ diffusion and adsorption. The use of EDOT as the reductant has been reported in the literature.[40,41] Only NPs were formed because the relatively weak coordination power of the sulfur atom in PEDOT could not restrain growth of the metal nuclei in the early stages. In this study, Au(III) and Ag(I) ions were preadsorbed on the α-MnO$_2$ NWs. The immobilization of gold and silver precursors limited the growth of Au and Ag species formed during (heterogeneous) reduction, thereby allowing NCs to be formed with PEDOT as the capping agent.

Figure 1 shows the typical transmission electron microscopy (TEM) images of as-synthesized Au−MnO$_2$ and Ag−MnO$_2$ catalysts. The MnO$_2$ NW surface was uniformly decorated with Au and Ag NCs with relatively narrow size distributions. The average size of the Au NCs (the black dots on the surface of the MnO$_2$ NWs in Figure 1A) was ∼0.9 nm, with a standard deviation of 0.2 nm. By comparison, the Ag NCs were larger in size (∼1.7 nm on the average) and broader in size distribution (standard deviation of 0.5 nm). Most of the Ag NCs were in the 1.5 to 2.0 nm size range, but there were a few 2−5 nm Ag NPs. The larger Ag NPs were also oval rather than spherical in shape (Figure 1B). This was distinctively different from the case of Au NCs where no NC agglomeration was observed. The difference in shape and size of the Au and Ag NCs could be due to their different affinity for the capping agent. It may be concluded that PEDOT is a good capping agent for the Au NCs and is not as effective in protecting the Ag NCs.
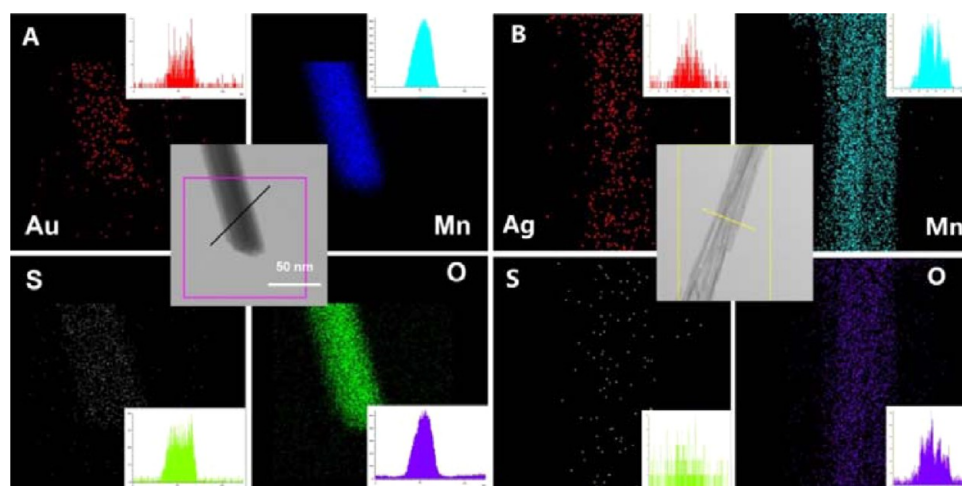
Figure 2. Elemental maps of Au, Mn, S, and O for (A) Au−MnO$_2$ and (B) Ag−MnO$_2$.

The elemental distributions in Au−MnO$_2$ and Ag−MnO$_2$ were assayed by scanning transmission electron microscopy (STEM, Figure 2). The resulting elemental maps confirmed the uniform dispersion of Au NCs and Ag NCs in the MnO$_2$ NWs. The S/Au and S/Ag ratios were, however, different for the PEDOT-protected Au and Ag NCs (Figure 2). The higher S/Au ratio confirms the stronger affinity between Au and PEDOT resulting in greater protection of the Au NCs by PEDOT, and consequently, lesser NC aggregation than in the case of PEDOT-protected Ag NCs.

High resolution X-ray photoelectron spectroscopy (XPS) was used to analyze the surface compositions and electronic interactions in Au−MnO$_2$ and Ag−MnO$_2$ (Figure S3, Supporting Information). The two Au XPS peaks at 83.5 and 87.2 eV correspond well with the binding energies of Au 4f$_{7/2}$ and Au 4f$_{5/2}$ electrons, respectively.[32,42] The Au 4f$_{7/2}$ peak could be deconvoluted into two component peaks assignable to the reduced Au(0) clusters (83.5 eV) and Au(I) ions (84.3 eV). In the Ag 3d region of Ag−MnO$_2$, the two peaks with binding energies at 367.5 and 373.6 eV are assignable to Ag(0) 3d$_{5/2}$ and Ag(0) 3d$_{3/2}$, respectively.[43,44] The Ag 3d peaks could also be further deconvoluted. For example, the Ag 3d$_{5/2}$ peak could be deconvoluted into two component peaks associated with Ag(I) (367.5 eV) and Ag(0) (368.2 eV).[43] The Mn 2p$_{3/2}$ peak at 642.0 eV and the Mn 2p$_{1/2}$ peak at 653.7 eV confirm that Mn existed as MnO$_2$ (Figure S4A, Supporting Information).[45] However, a comparison of the Mn 2p$_{3/2}$ peaks of α-MnO$_2$ NWs, Au−MnO$_2$, and Ag−MnO$_2$ revealed some binding energy shifts among them (Figure S4B, Supporting Information). The binding energy of Mn 2p$_{3/2}$ was 641.4 eV in Au−MnO$_2$ and 641.8 eV in Ag−MnO$_2$. These values represent down shifts of 0.62 and 0.22 eV from the MnO$_2$ NWs (642.0 eV), respectively. The binding energy shifts of the Mn 2p region suggest electron migration from the metal NCs to the manganese oxide and hence the existence of metal−support interaction between MnO$_2$ NWs and noble metal NCs. Metal−support interaction between noble metals and MnO$_x$ has previously been reported for Au NPs in CO oxidation.[36] From the magnitudes of the shift, the interaction was apparently stronger in Au−MnO$_2$. The wt % values of Au and Ag species in the hybrids, as measured by the relative integrated peak intensifies, were 13.4% and 11.6%, respectively. The smaller number of the latter is yet another indication of a weaker metal−support interaction.

The catalysts were tested in Li−O$_2$ full cells using 1 M LiCF$_3$SO$_3$ solution in TEGDME as the electrolyte. The test window of 2.2 to 4.4 V was set, to avoid electrolyte decomposition.[46] Figure 3 shows the first cycle discharge−
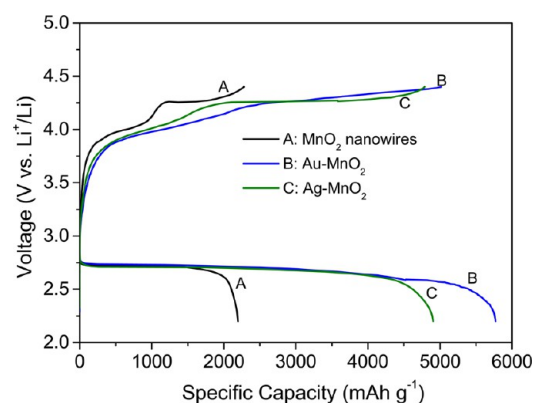

Figure 3. Full-cell discharge−charge curves with different cathode catalysts: (A) α-MnO$_2$ NWs; (B) Au−MnO$_2$, and (C) Ag−MnO$_2$. The current density used in the measurements was 100 mA g^{-1}.

charge curves of three cells at the current density of 100 mA g^{-1}, which differed only in the cathode catalyst used (α-MnO$_2$ NWs, Au−MnO$_2$, and Ag−MnO$_2$). The performance of the α-MnO$_2$ NW catalyst was similar to that reported by Bruce and co-workers.[13] On the other hand, cells with Au−MnO$_2$ or Ag−MnO$_2$ cathode catalyst showed higher capacities and smaller voltage gaps. Specifically, discharge and charge capacities were 5759 and 5020 mAh g^{-1} for the Au−MnO$_2$ cell, 4903 and 4800 mAh g^{-1} for the Ag−MnO$_2$ cell, and only 2182 and 2286 mAh g^{-1} for the α-MnO$_2$ NW cell. The discharge and charge capacities of the Au−MnO$_2$ cell were therefore ∼2.6 and ∼2.2 times those of the α-MnO$_2$ NW cell. Furthermore, at the specific capacity of 1000 mAh g^{-1}, the charge−discharge voltage gap was 1.24 V for the Au−MnO$_2$ cell, 1.29 V for the Ag−MnO$_2$ cell, and a much higher 1.42 V for the α-MnO$_2$ NW cell. The addition of noble metal NCs to α-MnO$_2$ was able to reduce the charge−discharge voltage gap by as much as 180 mV. The activation overpotentials in discharge were about the same for all three cells; and hence the reduced voltage gaps were due mainly to the improvement of OER kinetics in the presence of Au and Ag NCs. It should be mentioned that the

cells in this study were fully discharged and charged in the tests. The Au−MnO$_2$ cell compared favorably to previous studies where noble metal catalysts were evaluated under similar testing conditions (e.g., ~2.6 nm Pd NPs on carbon):[6] namely, a higher capacity (5759 vs ~2700 mAh g^{-1} for the Pd−C catalyst) and a lower OER voltage (3.73 vs 4.2 V at 250 mAh.g^{-1} for the Pd−C catalyst).[6] Furthermore, the addition of Au and Ag NCs also increased the round-trip efficiency. The round-trip efficiencies calculated based on 1st cycle measurements were 68.8%, 67.8%, and 65.5% for Au−MnO$_2$, Ag−MnO$_2$ and α-MnO$_2$ NWs, respectively. It should be mentioned that many round-trip efficiencies of lithium−oxygen cells in the literature were tested at 5−15% of the full cell capacity only[47,48] Based on these observations, the effectiveness of the three catalysts at 100 mAh g^{-1} may be ranked in the following order: Au−MnO$_2$ > Ag−MnO$_2$ > α-MnO$_2$ NWs. The first cycle discharge products were characterized by XPS (Figure S5, Supporting Information), and Li$_2$O$_2$ was the only discharge product detected for all three electrodes.[49,50]

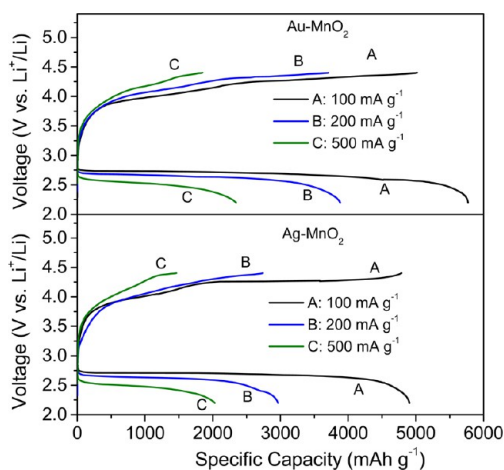The rate performance of cells with Au−MnO$_2$ or Ag−MnO$_2$ cathode catalyst was then compared (Figure 4). The trend of

Figure 4. Discharge−charge curves of cells with Au−MnO$_2$ and Ag−MnO$_2$ cathode catalysts at different current densities in the 2.2 to 4.4 V voltage window.

increasing discharge and charge polarizations with increased current density was the same for the two cells. At the same current density, the Au−MnO$_2$ cell always provided a higher capacity than the Ag−MnO$_2$ cell. For the depth of discharge (DOD) of 1300 mAh g^{-1}, the charge−discharge voltage gaps were 1.32 V at 100 mA g^{-1}, 1.49 V at 200 mA g^{-1}, and 1.85 V at 500 mA g^{-1} for the Au−MnO$_2$ cell. The corresponding values for the Ag−MnO$_2$ cell were 1.43, 1.57, and 1.98 V. It may therefore be concluded that the Au−MnO$_2$ catalyst had higher ORR and OER catalytic activities. Other than a smaller charge−discharge voltage gap, the Au−MnO$_2$ cell also delivered 18%, 31%, and 15% more capacity than the Ag−MnO$_2$ cell at the current density of 100, 200, and 500 mA g^{-1}, respectively. All of these are testimony of the higher catalytic activities of the Au−MnO$_2$ catalyst for oxygen electrocatalysis.

For stability evaluation, cells with Au−MnO$_2$, Ag−MnO$_2$, and α-MnO$_2$ NW cathode catalysts were cycled at a current density of 100 mA g^{-1} to a capacity of 1000 mAh g^{-1} (Figure 5). The voltages at the end of discharge and charge were recorded and compared. Among the three cells, the cell with Au−MnO$_2$ cathode catalyst had the best cycling performance;

showing little variation in capacity over 60 cycles. The end-of-discharge voltage was nearly constant throughout the cycling (at 2.7 V) but there was a graduate increase in the end-of-charge voltage with cycling. The end-of-charge voltage was lower than 4.4 V for the first 30 cycles but increased to 4.5 V in the 40th cycle and to 4.62 V in the 60th cycle. Different from the Au−MnO$_2$ cell, the Ag−MnO$_2$ cell cycled less stably, the end-of-charge and end-of-discharge voltages were 4.40 and 2.73 V in the 10th cycle and increased to 4.59 and 2.41 V by the 15th cycle. The α-MnO$_2$ cell had the worst stability; showing severely increasing polarizations during cycling. The end-of-discharge and end-of-charge voltages were as high as 2.68 and 4.41 V, respectively, even in the 2nd cycle. These values escalated to 1.42 and 4.72 V by the 6th cycle, with the latter close to the electrolyte decomposition voltage (4.78 V). Therefore, at the same current density, the cell with Au−MnO$_2$ catalyst outperformed the cells with the other two catalysts in terms of cycle stability.

The performance of the Au−MnO$_2$ catalyst was also benchmarked against the best of α-MnO$_2$-based hybrid catalysts in the literature. Both higher specific capacity and greater cycle stability were shown under comparable conditions in the full cell test (5759 mAh g^{-1} at 100 mA g^{-1} vs 2304 mAh g^{-1} at 60 mA g^{-1}; over 60 cycles at a depth of discharge of 1000 mAh g^{-1} vs 25 cycles at DOD of 600 mAh g^{-1}).[51]

To gain some insights into the discharge and charge processes, several electrodes were fabricated, discharged and charged at 100 mA g^{-1} to representative end points (2.2, 4.0, 4.2, and 4.4 V), dismantled from the cell, and had their morphology examined (Figures 6−8). Figure 6A shows that, at the end of discharge to 2.2 V, the entire surface of the Au−MnO$_2$ electrode was covered with a leaf-like Li$_2$O$_2$ solid with the longer diameter being ~400 nm. No NW structure could be seen. The Li$_2$O$_2$ layer became thinner after charging 4.0 V, exposing some of the underlying wire-like morphology (Figure 6B) as a result of the partial decomposition of Li$_2$O$_2$. When the charge potential was raised to 4.2 V, most of the Li$_2$O$_2$ solid coating disappeared, revealing more NWs with smoother surfaces. This is indication of the almost complete decomposition of Li$_2$O$_2$ at this higher voltage (Figure 6C). Finally, all solid discharge product completely disappeared with full restoration of the NW architecture after charging to 4.4 V (Figure 6D). Because prevailing views consider Li$_2$O$_2$ formation as the only reversible reaction in the Li−O$_2$ cathode, the complete disappearance of the solid discharge product suggests Li$_2$O$_2$ instead of Li$_2$O as the main reaction product. It should be empathized that the decomposition of the discharge product on the surface of the Au−MnO$_2$ catalyst was almost complete at 4.2 V.

The morphology evolution of the Ag−MnO$_2$ catalyst was likewise followed at preselected discharge and charge voltages. The Ag−MnO$_2$ surface was covered with a porous continuous solid Li$_2$O$_2$ after discharge to 2.2 V. The solid deposit, which was thicker than the reaction product on Au−MnO$_2$, which had a knobby appearance consisting of many interlinked spherical particles (Figure 7A). The solid product was thinner and less knobby at 4.0 V but the Ag−MnO$_2$ surface was still fully covered (Figure 7B). The amount of irregular solids on the electrode surface decreased significantly at 4.2 V, resulting in the reappearance of the NW morphology. Despite the disappearance of the spherical particles, many parts of the electrode surface were still covered by a thin film (Figure 7C). The solid deposit was only completely removed after charging
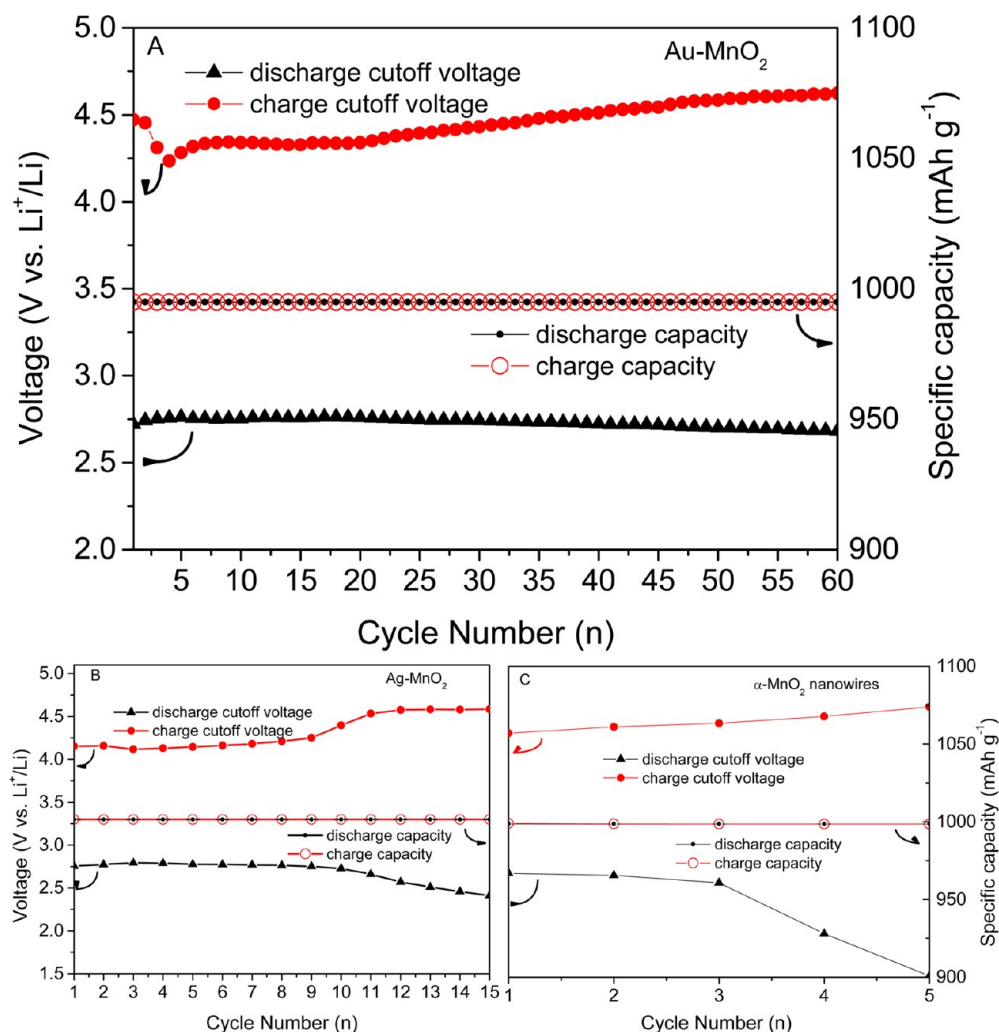
Figure 5. Cycle stability of cells with different cathode catalysts. (A) Au−MnO$_2$, (B) Ag−MnO$_2$, and (C) MnO$_2$ NWs. The measurements were performed at a current density of 100 mA g^{-1} to a DOD of 1000 mAh g^{-1}.

to 4.4 V. The total disappearance of the solid deposit signified the complete decomposition of the discharge product (Figure 7D). However, a higher voltage (4.4 V) was required in this case relative to product decomposition on Au−MnO$_2$.

The cell with the pristine α-MnO$_2$ NW cathode exhibited a similar discharge product morphology as the Ag−MnO$_2$ cell (Figure 8A). The discharge product consisted of thick agglomerates of spherical particles with pores between them. The solid layer was still quite thick even after charging to 4.0 V (Figure 8B). Thinning of the solid layer occurred after charging to 4.2 V, but the surface of the NWs was still fully covered with a solid deposit (Figure 8C). The solid product, however, disappeared completely after charging to 4.4 V with full restoration of the NW appearance. Similar to the Ag−MnO$_2$ catalyst, the complete decomposition of the discharge product also required a higher charge voltage of 4.4 V. In summary, Figures 6−8 show that 4.4 V was a high enough voltage to restore the catalyst original morphology. The discharge product morphology varied most noticeably at 4.2 V due to the different extents of Li$_2$O$_2$ decomposition. Nearly all of the solid Li$_2$O$_2$ was decomposed on the Au−MnO$_2$ electrode. Slightly more than half of Li$_2$O$_2$ was decomposed on the Ag−MnO$_2$ electrode, and only a small fraction of Li$_2$O$_2$ was decomposed on the α-MnO$_2$ NW electrode.

There are three likely reasons for the good performance of the Au−MnO$_2$ and Ag−MnO$_2$ catalysts. First, Au and Ag clusters improve the ORR kinetics during discharge. The large number of uncoordinated surface atoms in Au and Ag clusters is a hotbed of catalytically active sites. Indeed, the experimental measurements in this study show that Au/Ag NCs deposited on a MnO$_2$ MW surface benefits the OER kinetics the most. Second, the hybrid surface is covered with the capping agent PEDOT, a conducting polymer that could facilitate the charge transfer in ORR/OER by lowering the resistance to electron transport. Last but not least, the Au and Ag clusters could also affect the morphology of the reaction product during discharge. The formation and decomposition of discharge products is closely associated with Li$^+$ and O$_2$ transfer processes, which determine the cathode capacity and cycling performance. The morphology evolution measurements revealed that Au clusters tend to promote the formation of leaf-like discharge products, which are easier to decompose during charging; and hence are more able to provide a higher capacity, higher round-trip efficiency and a longer cycle life. The Ag clusters, although not as good as the Au clusters, are still more effective in decomposing the discharge products than pristine α-MnO$_2$ NWs.
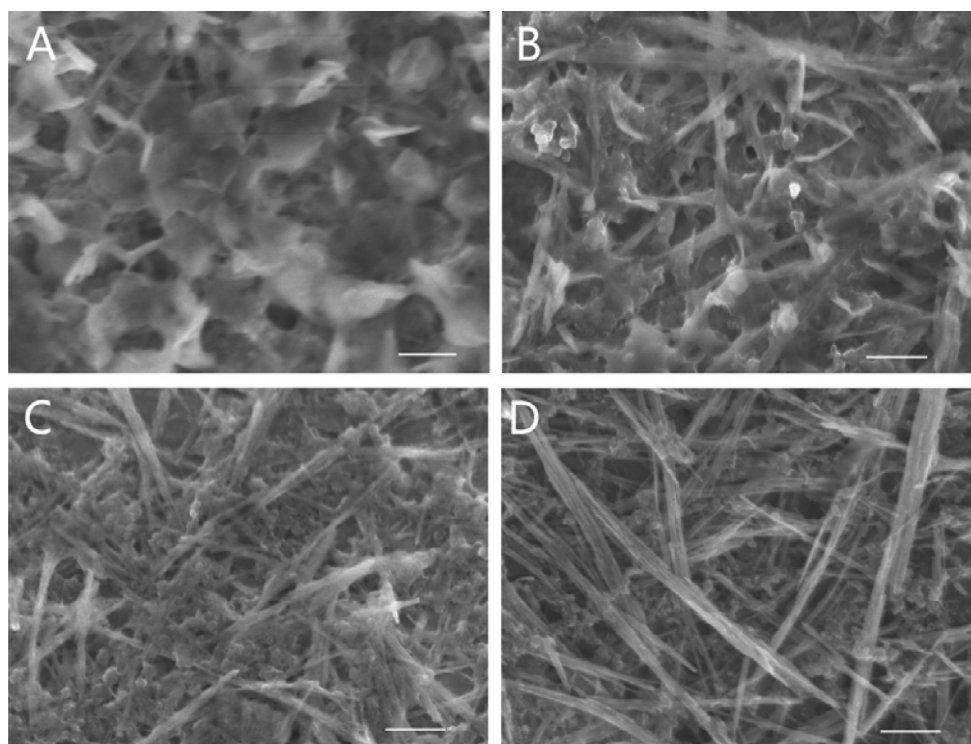
Figure 6. SEM images of the morphology of Au−MnO$_2$ in discharge−charge operations at 100 mA g^{-1}. (A) At the end-of-discharge (2.2 V), (B) after charging to 4.0 V, (C) after charging to 4.2 V, and (D) after charging to 4.4 V. (The scale bar is 500 nm.)
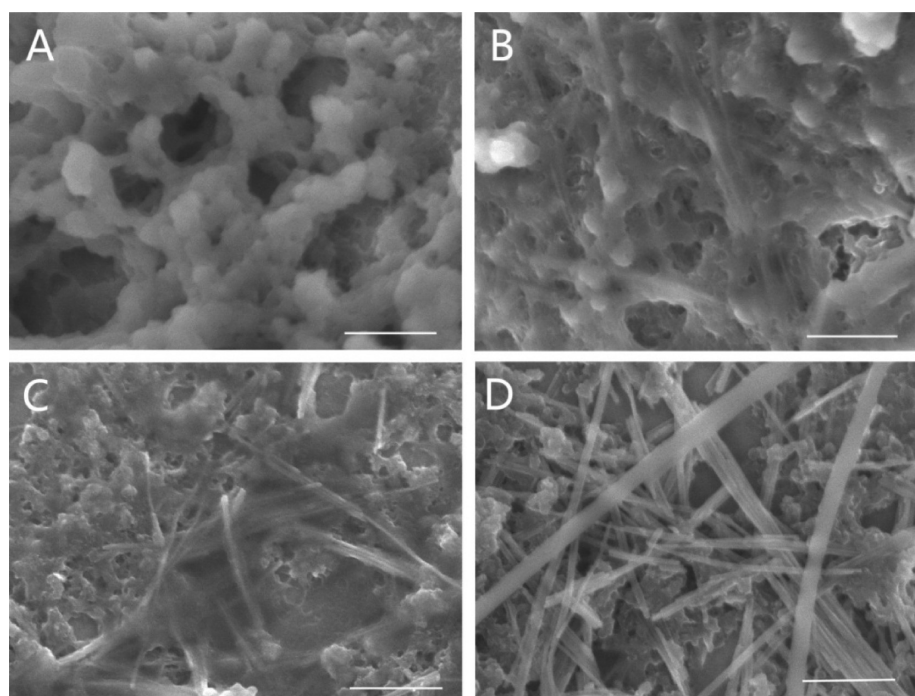

Figure 7. SEM images of the morphology of Ag−MnO$_2$ discharged and charged at 100 mA g^{-1}. (A) After discharging to 2.2 V, (B) after charging to 4.0 V, (C) after charging to 4.2 V, and (D) after charging to 4.4 V. (The scale bar is 500 nm.)

3. CONCLUSIONS

PEDOT-protected Au/Ag NC-MnO$_2$ NW hybrids were evaluated for their effectiveness in ORR and OER in nonaqueous electrolyte. Performance testing was carried out in lithium−oxygen test cells using the Au/Ag−MnO$_2$ as the cathode catalysts and benchmarked against the α-MnO$_2$ NW catalyst (the best of MnO$_2$ catalysts). The Au/Ag−MnO$_2$, especially the Au−MnO$_2$ catalyst, performed very well relative to the pristine α-MnO$_2$ NWs. The cell with the Au−MnO$_2$ catalyst could provide discharge and charge capacities of 5759 and 5020 mAh g^{-1}, and a voltage gap of 1.36 V at a current density of 100 mA g^{-1}. It also showed better rate performance and good cycle stability. The cell with the Au−MnO$_2$ as
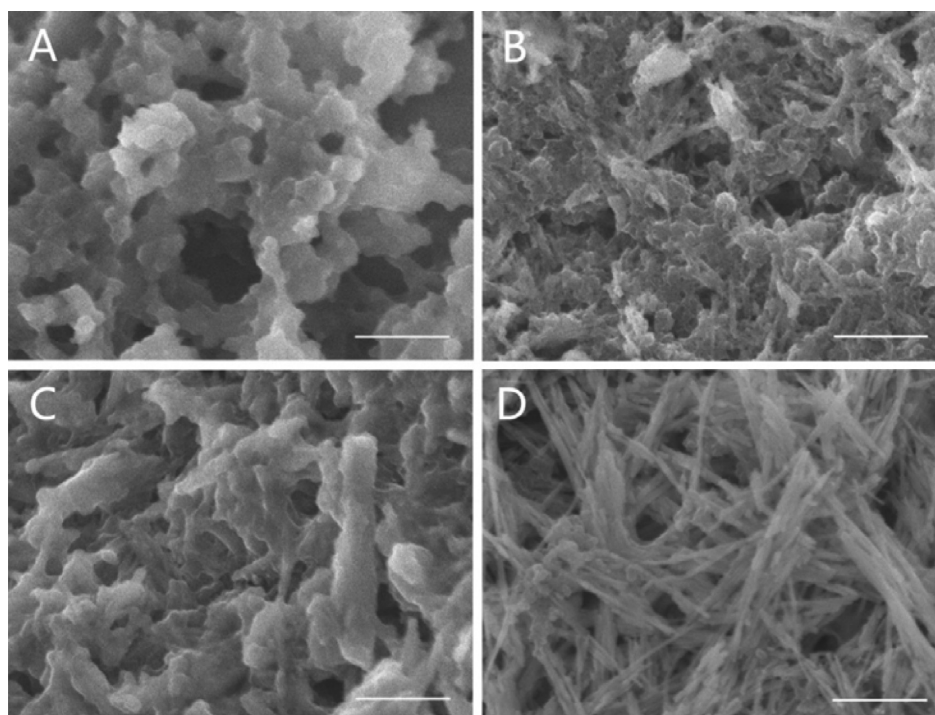
Figure 8. SEM images of the morphology of α-MnO$_2$ NWs discharged and charged at 100 mA g^{-1} to (A) 2.2 V, (B) 4.0 V, (C) 4.2 V, and (D) 4.4 V. (The scale bar is 500 nm.)

cathode catalyst could also run steadily for at least 60 cycles at 100 mA g^{-1}. The good full cell performance with the Au/Ag–MnO$_2$ catalyst is postulated to be due to the effectiveness of Au/Ag clusters in promoting the ORR/OER kinetics and the morphology of the discharge products on α-MnO$_2$ NWs. In addition, the conducting property of the PEDOT capping agent also contributed to kinetic enhancements by lowering the resistance to electron transport in the charge transfer processes at the cathode.

4. EXPERIMENTAL SECTION

Chemicals. Manganese acetate, polyvinylidene fluoride (PVDF), N-methyl-2-pyrrolidone (NMP), tetraethylene glycol dimethyl ether (TEGDME), lithium trifluoromethanesulfonate (LiCF$_3$SO$_3$), acetonitrile, hydrogen tetrachloroaurate rehydrates (HAuCl$_4$·3H$_2$O), silver nitrite (AgNO$_3$), 3,4-ethylenedioxythiophene (EDOT), manganese sulfate monohydrate (MnSO$_4$·H$_2$O), ammonium sulfate ((NH$_4$)$_2$SO$_4$), and ammonium persulfate ((NH$_4$)$_2$S$_2$O$_8$) were purchased from Sigma. Ketjen Black (Ketjen Black International, ECP600JD) was supplied by MTI. All chemicals were used as received.

Characterization. Field-emission transmission electron microscopy (FETEM) and electron diffraction were performed on a JEOL JEM-2010 microscope operating at 200 kV accelerating voltage. Samples for TEM analysis were prepared by dispensing a drop of the dilute catalyst dispersion in ethanol on an amorphous carbon-coated TEM copper grid. High resolution field-emission scanning electron microscopy (FESEM) was carried out on a JEOL JSM-6700F microscope operating at 5 kV accelerating voltage. Samples for FESEM analysis were prepared by dispensing several drops of the dilute catalyst dispersion in ethanol on a clean silicon (111) substrate. X-ray diffraction (XRD) patterns were recorded by a Bruker GADDS XRD powder diffractometer using a Cu Kα source (λ = 1.5418 Å) at 40 kV and 30 mA. Samples for XRD analysis were prepared in exactly the same way as the samples for FESEM analysis. X-ray photoelectron spectroscopy (XPS) analysis was carried out on a Kratos Axis Ultra DLD spectrometer. All binding energies were corrected by referencing the C 1s emission from adventitious carbon to 284.5 eV.

Electrode Preparation and Battery Tests. A catalyst ink was prepared by dispersing the catalyst of interest, Ketjen black and PVDF (in a 3:6:1 weight ratio) in NMP followed by overnight stirring. A measured amount of the ink was dispensed on a carbon disc (1.1 cm in diameter and 146 μm in thickness) and dried in a vacuum at 100 °C for 8 h. The catalyst loading on the carbon disc was ∼0.4–0.6 mg. The test batteries were (2032 button cells from MTI with perforations on the cathode casing) assembled from a catalyst-loaded carbon disc cathode, a Li metal pellet anode, a Whatman GF/B glass microfiber filter paper separator, and a 1 M LiCF$_3$SO$_3$ in TEGDEM electrolyte. Cell assembly was carried out in an Ar-filled glovebox where O$_2$ and moisture levels were below 1 ppm each. The perforations on the cathode casing were used for oxygen perfusion. After assembly, the coin cell was placed in a glass bottle fitted with a gas inlet and outlet. The bottle was sealed, removed from the glovebox, and purged with flowing pure O$_2$ (Soxal, 99.8%, H$_2$O < 3 ppm) at 1 atm for at least 15 min. The bottle was then sealed again. Battery testing was carried out on a Neware CT-3008 battery tester. Test cells were typically rested for 12 h before any electrochemical measurement. Current density was normalized by the combined weight of catalyst and Ketjen black carbon; and the cutoff voltages for discharge and charge were set at 2.2 and 4.4 V, respectively. Battery cycling was carried out at a current density of 100 mA g^{-1} to a depth of discharge 1000 mAh g^{-1}. The voltages at the end of discharge and charge were recorded.

For the examination of morphology evolution during discharge and charge, the catalyst ink composition was changed to 8:1:1 by weight. A Ni foam disc (1.1 cm diameter) replaced the carbon disc because the carbon fibers in the carbon paper were similar to MnO$_2$ NWs in appearance. After we tested with the desired conditions, the battery cell was disassembled and the Ni form disc was submerged in acetonitrile for at least 2 h. The Ni foam disc was then dried in a glovebox and examined by FESEM.

All capacity calculations reported in the following were based on the combined weight of catalyst and Ketjen black carbon. All electrode potentials in this study were referenced to Li$^+$/Li.

Synthesis of α-MnO$_2$ NWs. The synthesis of α-MnO$_2$ NWs was based a previously reported method.[52] In brief, manganese sulfate monohydrate (MnSO$_4$·H$_2$O, 8 mmol), ammonia sulfate ((NH$_4$)$_2$SO$_4$, 24 mmol), and ammonium persulfate ((NH4)$_2$S$_2$O$_8$, 8 mmol) were

dissolved in deionized water (DI water) at room temperature to form a clear solution. The solution was transferred to a Teflon-lined stainless steel autoclave and heated at 120 °C for 12 h. The resultant black precipitate was filtered off, washed with DI water thrice, and then vacuum-dried at 80 °C overnight.

Synthesis of Au Cluster-α-MnO$_2$ NW (Au−MnO$_2$) and Ag Cluster-α-MnO$_2$ NW (Ag−MnO$_2$) Hybrids. *Au−MnO$_2$.* 2 mL of 40 mM α-MnO$_2$ NWs (on a Mn atom basis) was mixed with 2 mL of 10 mM HAuCl$_4$ under moderate stirring (~500 rpm). Adsorption was allowed to continue for hours before the mixture was centrifuged at 5000 rpm for 5 min. The recovered solid residue was redispersed in 4 mL of ultrapure water, and added with 4 mL of 20 mM EDOT solution in 50% v/v water/ethanol mixture. The reduction reaction was carried out under stirring (~500 rpm) for 20 h. The final product was recovered from the reaction mixture by centrifugation (5000 rpm for 5 min).

Ag−MnO$_2$. The same procedure for the preparation of Au NCs on MnO$_2$ NWs was followed except that 2 mL of 10 mM HAuCl$_4$ was replaced with 2 mL of 10 mM AgNO$_3$.

■ ASSOCIATED CONTENT

Ⓢ Supporting Information

TEM, FESEM, and XPS of the Au/Ag NC-MnO$_2$ NW hybrids. This material is available free of charge via the Internet at http://pubs.acs.org.

■ AUTHOR INFORMATION

Corresponding Author

*J. Y. Lee. E-mail: cheleejy@nus.edu.sg.

Notes

The authors declare no competing financial interest.

■ ACKNOWLEDGMENTS

■ REFERENCES

(1) Bruce, P. G.; Freunberger, S. A.; Hardwick, L. J.; Tarascon, J.-M. Li-O$_2$ and Li-S Batteries with High Energy Storage. *Nat. Mater.* **2012**, *11*, 19−29.

(2) Wang, J.; Li, Y.; Sun, X. Challenges and Opportunities of Nanostructured Materials for Aprotic Rechargeable Lithium−Air Batteries. *Nano Energy* **2013**, *2*, 443−467.

(3) Girishkumar, G.; McCloskey, B.; Luntz, A. C.; Swanson, S.; Wilcke, W. Lithium - Air Battery: Promise and Challenges. *J. Phys. Chem. Lett.* **2010**, *1*, 2193−2203.

(4) Lu, Y. C.; Xu, Z.; Gasteiger, H. A.; Chen, S.; Hamad-Schifferli, K.; Shao-Horn, Y. Platinum-Gold Nanoparticles: A Highly Active Bifunctional Electrocatalyst for Rechargeable Lithium-Air Batteries. *J. Am. Chem. Soc.* **2010**, *132*, 12170−12171.

(5) Yilmaz, E.; Yogi, C.; Yamanaka, K.; Ohta, T.; Byon, H. R. Promoting Formation of Noncrystalline Li$_2$O$_2$ in the Li-O$_2$ Battery with RuO$_2$ Nanoparticles. *Nano Lett.* **2013**, *13*, 4679−4684.

(6) Lu, J.; Lei, Y.; Lau, K. C.; Luo, X.; Du, P.; Wen, J.; Assary, R. S.; Das, U.; Miller, D. J.; Elam, J. W.; Albishri, H. M.; El-Hady, D. A.; Sun, Y. K.; Curtiss, L. A.; Amine, K. A Nanostructured Cathode Architecture for Low Charge Overpotential in Lithium-Oxygen Batteries. *Nat. Commun.* **2013**, *4*, 2383.

(7) Lei, Y.; Lu, J.; Luo, X.; Wu, T.; Du, P.; Zhang, X.; Ren, Y.; Wen, J.; Miller, D. J.; Miller, J. T.; Sun, Y. K.; Elam, J. W.; Amine, K. Synthesis of Porous Carbon Supported Palladium Nanoparticle Catalysts by Atomic Layer Deposition: Application for Rechargeable Lithium-O$_2$ Battery. *Nano Lett.* **2013**, *13*, 4182−4189.

(8) Sun, B.; Munroe, P.; Wang, G. Ruthenium Nanocrystals as Cathode Catalysts for Lithium-Oxygen Batteries with a Superior Performance. *Sci. Rep.* **2013**, *3*, 2247.

(9) Jung, H. G.; Jeong, Y. S.; Park, J. B.; Sun, Y. K.; Scrosati, B.; Lee, Y. J. Ruthenium-based Electrocatalysts Supported on Reduced Graphene Oxide for Lithium-Air Batteries. *ACS Nano* **2013**, *7*, 3532−3539.

(10) Kim, B. G.; Kim, H. J.; Back, S.; Nam, K. W.; Jung, Y.; Han, Y. K.; Choi, J. W. Improved Reversibility in Lithium-Oxygen Battery: Understanding Elementary Reactions and Surface Charge Engineering of Metal Alloy Catalyst. *Sci. Rep.* **2014**, *4*, 4225.

(11) Ryu, W. H.; Yoon, T. H.; Song, S. H.; Jeon, S.; Park, Y. J.; Kim, I. D. Bifunctional Composite Catalysts Using Co$_3$O$_4$ Nanofibers Immobilized on Nonoxidized Graphene Nanoflakes for High-capacity and Long-Cycle Li-O$_2$ Batteries. *Nano Lett.* **2013**, *13*, 4190−4197.

(12) Zhao, G.; Xu, Z.; Sun, K. Hierarchical Porous Co$_3$O$_4$ Films as Cathode Catalysts of Rechargeable Li-O$_2$ Batteries. *J. Mater. Chem. A* **2013**, *1*, 12862−12867.

(13) Debart, A.; Paterson, A. J.; Bao, J.; Bruce, P. G. α-MnO$_2$ Nanowires: A Catalyst for the O$_2$ Electrode in Rechargeable Lithium Batteries. *Angew. Chem., Int. Ed.* **2008**, *47*, 4521−4524.

(14) Wang, L.; Zhao, X.; Lu, Y.; Xu, M.; Zhang, D.; Ruoff, R. S.; Stevenson, K. J.; Goodenough, J. B. CoMn$_2$O$_4$ Spinel Nanoparticles Grown on Graphene as Bifunctional Catalyst for Lithium-Air Batteries. *J. Electrochem. Soc.* **2011**, *158*, A1379−A1382.

(15) Zhang, L.; Zhang, S.; Zhang, K.; Xu, G.; He, X.; Dong, S.; Liu, Z.; Huang, C.; Gu, L.; Cui, G. Mesoporous NiCo$_2$O$_4$ Nanoflakes as Electrocatalysts for Rechargeable Li-O$_2$ Batteries. *Chem. Commun.* **2013**, *49*, 3540−3542.

(16) Hung, T. F.; Mohamed, S. G.; Shen, C. C.; Tsai, Y. Q.; Chang, W. S.; Liu, R. S. Mesoporous ZnCo$_2$O$_4$ Nanoflakes with Bifunctional Electrocatalytic Activities toward Efficiencies of Rechargeable Lithium-Oxygen Batteries in Aprotic Media. *Nanoscale* **2013**, *5*, 12115−12119.

(17) Suntivich, J.; Gasteiger, H. A.; Yabuuchi, N.; Nakanishi, H.; Goodenough, J. B.; Shao-Horn, Y. Design Principles for Oxygen-Reduction Activity on Perovskite Oxide Catalysts for Fuel Cells and Metal−Air Batteries. *Nat. Chem.* **2011**, *3*, 546−550.

(18) Jung, K. N.; Jung, J. H.; Im, W. B.; Yoon, S.; Shin, K. H.; Lee, J. W. Doped Lanthanum Nickelates with a Layered Perovskite Structure as Bifunctional Cathode Catalysts for Rechargeable Metal-Air Batteries. *ACS Appl. Mater. Interfaces* **2013**, *5*, 9902−9907.

(19) Xu, J. J.; Xu, D.; Wang, Z. L.; Wang, H. G.; Zhang, L. L.; Zhang, X. B. Synthesis of Perovskite-based Porous La$_{0.75}$Sr$_{0.25}$MnO$_3$ Nanotubes as a Highly Efficient Electrocatalyst for Rechargeable Lithium-Oxygen Batteries. *Angew. Chem., Int. Ed.* **2013**, *52*, 3887−3890.

(20) Kitaura, H.; Zhou, H. Electrochemical Performance of Solid-State Lithium-Air Batteries Using Carbon Nanotube Catalyst in the Air Electrode. *Adv. Energy Mater.* **2012**, *2*, 889−894.

(21) Lim, H. D.; Park, K. Y.; Song, H.; Jang, E. Y.; Gwon, H.; Kim, J.; Kim, Y. H.; Lima, M. D.; Ovalle Robles, R.; Lepro, X.; Baughman, R. H.; Kang, K. Enhanced Power and Rechargeability of a Li-O$_2$ Battery Based on a Hierarchical-Fibril CNT Electrode. *Adv. Mater.* **2013**, *25*, 1348−1352.

(22) Zhang, W.; Zhu, J.; Ang, H.; Zeng, Y.; Xiao, N.; Gao, Y.; Liu, W.; Hng, H. H.; Yan, Q. Binder-free Graphene Foams for O$_2$ Electrodes of Li-O$_2$ Batteries. *Nanoscale* **2013**, *5*, 9651−9658.

(23) Yoo, E.; Zhou, H. Li-Air Rechargeable Battery Based on Metal-free Graphene Nanosheet Catalysts. *ACS Nano* **2011**, *5*, 3020−3026.

(24) Nie, H.; Zhang, H.; Zhang, Y.; Liu, T.; Li, J.; Lai, Q. Nitrogen Enriched Mesoporous Carbon as a High Capacity Cathode in Lithium-Oxygen Batteries. *Nanoscale* **2013**, *5*, 8484−8487.

(25) Li, J.; Zhang, H.; Zhang, Y.; Wang, M.; Zhang, F.; Nie, H. A Hierarchical Porous Electrode Using a Micron-Sized Honeycomb-like Carbon Material for High Capacity Lithium-Oxygen Batteries. *Nanoscale* **2013**, *5*, 4647−4651.

(26) Park, J. B.; Lee, J.; Yoon, C. S.; Sun, Y. K. Ordered Mesoporous Carbon Electrodes for Li-O$_2$ Batteries. *ACS Appl. Mater. Interfaces* **2013**, *5*, 13426−12431.

(27) Li, F.; Ohnishi, R.; Yamada, Y.; Kubota, J.; Domen, K.; Yamada, A.; Zhou, H. Carbon Supported TiN Nanoparticles: An Efficient Bifunctional Catalyst for Non-aqueous Li-O₂ Batteries. *Chem. Commun.* **2013**, *49*, 1175−1177.

(28) Dong, S.; Chen, X.; Zhang, K.; Gu, L.; Zhang, L.; Zhou, X.; Li, L.; Liu, Z.; Han, P.; Xu, H.; Yao, J.; Zhang, C.; Zhang, X.; Shang, C.; Cui, G.; Chen, L. Molybdenum Nitride based Hybrid Cathode for Rechargeable Lithium-O₂ Batteries. *Chem. Commun.* **2011**, *47*, 11291.

(29) Li, G.; Jin, R. C. Atomically Precise Gold Nanoclusters as New Model Catalysts. *Acc. Chem. Res.* **2013**, *46*, 1749−1758.

(30) Chen, W.; Chen, S. Oxygen Electroreduction Catalyzed by Gold Nanoclusters: Strong Core Size Effects. *Angew. Chem., Int. Ed* **2009**, *48*, 4386−4389.

(31) Jeyabharathi, C.; Kumar, S. S.; Kiruthika, G. V.; Phani, K. L. Aqueous CTAB-Assisted Electrodeposition of Gold Atomic Clusters and Their Oxygen Reduction Electrocatalytic Activity in Acid Solutions. *Angew. Chem., Int. Ed* **2010**, *49*, 2925−2928.

(32) Negishi, Y.; Mizuno, M.; Hirayama, M.; Omatoi, M.; Takayama, T.; Iwase, A.; Kudo, A. Enhanced Photocatalytic Water Splitting by BaLa₄Ti₄O₁₅ Loaded with Approximately 1 nm Gold Nanoclusters Using Glutathione-Protected Au₂₅ Clusters. *Nanoscale* **2013**, *5*, 7188−7192.

(33) Yin, H.; Tang, H.; Wang, D.; Gao, Y.; Tang, Z. Facile Synthesis of Surfactant-free Au Cluster/Graphene Hybrids for High-Performance Oxygen Reduction Reaction. *ACS Nano* **2012**, *6*, 8288−8297.

(34) Lu, Y. Z.; Chen, W. Size Effect of Silver Nanoclusters on Their Catalytic Activity for Oxygen Electro-reduction. *J. Power Sources* **2012**, *197*, 107−110.

(35) El-Deab, M. S.; Ohsaka, T. Electrocatalytic Reduction of Oxygen at Au Nanoparticles-Manganese Oxide Nanoparticle Binary Catalysts. *J. Electrochem. Soc.* **2006**, *153*, A1365−A1371.

(36) Longo, A.; Liotta, L. F.; Carlo, G. D.; Giannici, F.; Venezia, A. M.; Martorana, A. Structure and the Metal Support Interaction of the Au/Mn Oxide Catalysts. *Chem. Mater.* **2010**, *22*, 3952−3960.

(37) Gorlin, Y.; Chung, C. J.; Benck, J. D.; Nordlund, D.; Seitz, L.; Weng, T. C.; Sokaras, D.; Clemens, B. M.; Jaramillo, T. F. Understanding Interactions between Manganese Oxide and Gold That Lead to Enhanced Activity for Electrocatalytic Water Oxidation. *J. Am. Chem. Soc.* **2014**, *136*, 4920−4926.

(38) Goh, F. W. T.; Liu, Z. L.; Ge, X. M.; Zong, Y.; Du, G. J.; Hor, T. S. A. Ag Nanoparticle-Modified MnO₂ Nanorods Catalyst for Use as an Air Electrode in Zinc-Air Battery. *Electrochim. Acta* **2013**, *114*, 598−604.

(39) Tang, Q. E.; Jiang, L. H.; Qi, J.; Jiang, Q.; Wang, S. L.; Sun, G. Q. One Step Synthesis of Carbon-Supported Ag/MnᵧOₓ Composites for Oxygen Reduction Reaction in Alkaline Media. *Appl. Catal., B* **2011**, *104*, 337−345.

(40) Hong, J. Y.; Huh, S. Facile Preparation of SERS-Active Nanostructured Au Spheres by Simple Reduction of AuCl₄-ions with EDOT. *J. Colloid Interface Sci.* **2014**, *418*, 360−365.

(41) Kumar, S. S.; Kumar, C. S.; Mathiyarasu, J.; Phani, K. L. Stabilized Gold Nanoparticles by Reduction Using 3,4-Ethylenedioxythiophene-polystyrenesulfonate in Aqueous Solutions: Nanocomposite Formation, Stability, and Application in Catalysis. *Langmuir* **2007**, *23*, 3401−3408.

(42) Yao, Q. F.; Yu, Y.; Yuan, X.; Yu, Y.; Xie, J. P.; Lee, J. Y. Two-Phase Synthesis of Small Thiolate-Protected Au₁₅ and Au₁₈ Nanoclusters. *Small* **2013**, *9*, 2696−2701.

(43) Bootharaju, M. S.; Pradeep, T. Investigation into the Reactivity of Unsupported and Supported Ag₇ and Ag₈ Clusters with Toxic Metal Ions. *Langmuir* **2011**, *27*, 8134−8143.

(44) Yuan, X.; Yeow, T. J.; Zhang, Q. B.; Lee, J. Y.; Xie, J. P. Highly Luminescent Ag⁺ Nanoclusters for Hg²⁺ ion Detection. *Nanoscale* **2012**, *4*, 1968−1971.

(45) Jin, L.; Xu, L.; Morein, C.; Chen, C.-h.; Lai, M.; Dharmarathna, S.; Dobley, A.; Suib, S. L. Titanium Containing γ-MnO₂ (TM) Hollow Spheres: One-Step Synthesis and Catalytic Activities in Li/Air Batteries and Oxidative Chemical Reactions. *Adv. Funct. Mater.* **2010**, *20*, 3373−3382.

(46) Laoire, C. O.; Mukerjee, S.; Plichta, E. J.; Hendrickson, M. A.; Abraham, K. M. Rechargeable Lithium/TEGDME-LiPF₆/O₂ Battery. *J. Electrochem. Soc.* **2011**, *158*, A302−A308.

(47) Choi, R.; Jung, J.; Kim, G.; Song, K.; Kim, Y.-I.; Jung, S. C.; Han, Y.-K.; Song, H.; Kang, Y.-M. Ultra-low Overpotential and High Rate Capability in Li-O₂ Batteries through Surface Atom Arrangement of PdCu Nanocatalysts. *Energy Environ. Sci.* **2014**, *7*, 1362−1368.

(48) Jung, J.; Song, K.; Bae, D. R.; Lee, S. W.; Lee, G.; Kang, Y. M. Beta-FeOOH Nanorod Bundles with Highly Enhanced Round-Trip Efficiency and Extremely Low Overpotential for Lithium-Air Batteries. *Nanoscale* **2013**, *5*, 11845−11849.

(49) Du, P.; Lu, J.; Lau, K. C.; Luo, X.; Bareno, J.; Zhang, X.; Ren, Y.; Zhang, Z.; Curtiss, L. A.; Sun, Y.-K.; Amine, K. Compatibility of Lithium Salts with Solvent of the Non-aqueous Electrolyte in Li-O₂ Batteries. *Phys. Chem. Chem. Phys.* **2013**, *15*, 5572−5581.

(50) Qin, Y.; Lu, J.; Du, P.; Chen, Z.; Ren, Y.; Wu, T.; Miller, J. T.; Wen, J.; Miller, D. J.; Zhang, Z.; Amine, K. In Situ Fabrication of Porous-Carbon-Supported α-MnO₂ Nanorods at Room Temperature: Application for Rechargeable Li-O₂ Batteries. *Energy Environ. Sci.* **2013**, *6*, 519−531.

(51) Cao, Y.; Wei, Z.; He, J.; Zang, J.; Zhang, Q.; Zheng, M.; Dong, Q. α-MnO₂ Nanorods Grown in Situ on Graphene as Catalysts for Li-O₂ Batteries with Excellent Electrochemical Performance. *Energy Environ. Sci.* **2012**, *5*, 9765−9768.

(52) Wang, X.; Li, Y. D. Selected-Control Hydrothermal Synthesis of Alpha- and Beta-MnO₂ Single Crystal Nanowires. *J. Am. Chem. Soc.* **2002**, *124*, 2880−2881.